Coiling instability of multilamellar membrane tubes with anchored polymers

Ilan Tsafrir,[1] Marie-Alice Guedeau-Boudeville,[2] Daniel Kandel,[1] and Joel Stavans[1]
[1]*Department of Physics of Complex Systems, The Weizmann Institute of Science, Rehovot 76 100, Israel*
[2]*Laboratoire de Physique de la Matière Condensée, URA No. 792, Collège de France, 11 Place Marcelin Berthelot, F-75231 Paris Cedex 05, France*
(Received 29 August 2000; published 27 February 2001)

We study experimentally a coiling instability of cylindrical multilamellar stacks of phospholipid membranes, induced by polymers with hydrophobic anchors grafted along their hydrophilic backbone. Our system is unique in that coils form in the absence of both twist and adhesion. We interpret our experimental results in terms of a model in which local membrane curvature and polymer concentration are coupled. The model predicts the occurrence of maximally tight coils above a threshold polymer occupancy. A proper comparison between the model and experiment involved imaging of projections from simulated coiled tubes with maximal curvature and complicated torsions.

DOI: 10.1103/PhysRevE.63.031603 PACS number(s): 68.03.−g, 87.16.Dg

I. INTRODUCTION

Coiling is a common occurrence in vastly different systems and on many scales, ranging from carbon nanotubes [1] and DNA molecules [2] to telephone cords and tendrils of climbing plants [3]. The framework most commonly used to model coiling in these and other systems is that of an elastic rod. Buckling of the central line is explained by showing that converting twist to writhe lowers the elastic energy [4].

We study the coiling of cylindrical stacks of lipid membranes [5], called *myelin figures*, interacting with an amphiphilic polymer. This polymer has several hydrophobic side groups attached along a flexible hydrophilic backbone, which it inserts into the membranes in order to shield them from the surrounding water [6]. The membranes composing a myelin figure are in a two-dimensional liquid state, and therefore cannot support twist. Application of torque on the cylinder simply leads to flow of material around the tube. Thus the interplay between twist and writhe cannot explain the coiling observed in our experiments.

The existence and coiling of myelin figures has been observed as far back as 1854 [7] (see also [8]). More recently, similar shapes have been observed during the hydration of a surfactant by brine [9,10]. Coiling of myelin figures has also been reported for a system of egg-yolk lecithin [11–13]. This system is a mixture containing many different lipids, having a variety of tail lengths and degrees of saturation [14]. In another experiment it was shown that a binary mixture of dimyristoylphosphatidylcholine (DMPC) and cardiolipin forms single and double helices in the presence of calcium ions [15]. In these two studies, it was claimed that (i) the energy gained by surface adhesion overcomes the energy cost of bending a tube, and (ii) the tighter the coil, the longer the line of contact between tubes becomes, thus increasing the area of contact.

In contrast, our experiments clearly show that surface adhesion is negligible in our system. In order to account for coiling in our experiments, we present a simple model, in which we assume that polymer molecules locally induce spontaneous curvature. The coiling instability results from a coupling between local polymer concentration and membrane curvature. Within such a framework, hollow tubes may also undergo other shape instabilities such as pearling [6,16,17]. However, the constraints imposed by the geometry of the cylindrical membrane stack prevent them from occurring. Our model predicts the occurrence of maximally tight coils above a threshold polymer concentration. Indeed, only maximally curved coils were formed in our experiments. A theoretical analysis shows that virtual slices through maximally curved helices can be very similar to the observed images.

Section II describes the materials and methods used in our experiments. Section III describes the types of coils observed, and shows that adhesion does not play a major role in these experiments. Section IV presents the simple model that explains the major findings. First, a heuristic argument is given as to why such an approach works. Then the full mean-field calculation is given. Finally, Sec. V outlines the difficulties in comparing quantitatively the model and the experiment.

II. MATERIALS AND METHODS

Vesicles were made of stearoyl-oleoyl-phosphatidylcholine (SOPC) with C_{18} alkyl chains. The polymer used is hydrophilic dextran [molecular weight (MW) 162 000 g/mol] functionalized with both palmitoyl alkyl chains and dodecanoic nitrobenzoxadiazole NBD chains as fluorescent markers. The hydrophobic anchors, distributed statistically along the backbone (about 1 alkyl chain per 25 glucose units) are C_{16} long. On average there are about four persistence lengths between consecutive anchors. Therefore, the extension of each polymer molecule on the two-dimensional membrane is much larger than its extension into the third dimension. Events were observed by phase contrast microscopy and recorded on video. For fluorescence imaging the NBD markers were excited with argon laser illumination, and observed with a cooled charge-coupled device camera.

Samples were prepared by drying a 0.5–1.0 μl droplet of SOPC dissolved in a 4:1 chloroform-methanol solution (7.35 mg/ml) on a glass slide. The sample was then closed from the top and sides, and hydration was effected by injecting a

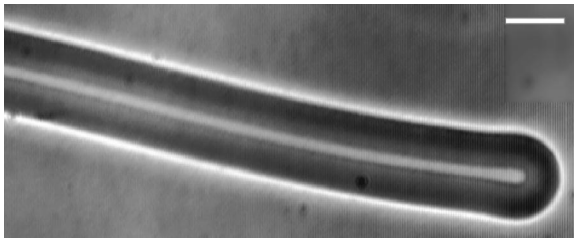

FIG. 1. Image of a myelin figure at very low polymer concentration. The scale bar represents 20 μm.

polymer solution of known concentration c_p into the closed cell. Some time after hydration, a variety of self-assembled structures formed, including myelin figures. All the structures observed in these experiments were still connected to a lipid reservoir, allowing exchange of material, including both lipids and polymer molecules. Experiments were conducted at room temperature, well above the solid-liquid transition for SOPC. This allowed free diffusion of anchored polymers along the membranes.

We stress that while the polymer concentration in solution, c_p, is known, we do not control the surface concentration on the bilayers. The slow evolution of some of the structures we observe is consistent with a possible variation of this concentration over time.

III. RESULTS

Electron micrographs of cross sections of myelin figures reveal that they are rodlike lyotropic liquid-crystalline structures containing a large number (hundreds to thousands) of concentric cylindrical membranes separated by thin hydration layers [12]. The smectic order in these stacks of membranes is not ideal, as many defects are present. The outer radius of a myelin figure can reach tens of micrometers, while the radius of the water core may be of the order of, or smaller than optical resolution (0.2 μm). The myelin figures, which are connected at one end to a large lipid reservoir, are continuously elongating. The rate of elongation of a myelin figure lies in the range of 0–0.3 μm/sec. Throughout the experiment, polymer molecules continue to anchor from the surrounding solution. Hence we assume that there is continuous accumulation of both lipid and polymer molecules.

Hydration of a patch of lipids by a polymer solution of small c_p results in the formation of myelin figures, which display a clear tendency to straighten over lengths many times larger than their diameter (see Fig. 1). As c_p is increased, myelin figures become more floppy and curved. For large enough values of c_p, a writhing instability sets in and tubes bend, forming irregular structures (Fig. 2), single helices [Fig. 3(a)], and double helices (Fig. 4). The type of coiled structure formed depends in great part on the dynamics of the formation process. By far the most common event is for the tip to begin to curve in upon itself forming a seemingly irregular ball-like structure (Fig. 2). However, when the ball is large enough, some sort of ordering can be seen [Fig. 5(e)]. Coils that start forming at their bases usually evolve into nearly ideal single helices. The uncoiled part of the tube leading to the tip is pulled in and wound around to

FIG. 2. When the instability begins at the tip, the tube loops back upon itself forming a globular structure. Such a structure is seen here (a) 0, (b) 83, (c) 109, (d) 155, (e) 221, and (f) 371 sec after onset of bending. The scale bar represents 10 μm.

form the next loop [18]. In cases where the coiling starts in the middle, it begins as a hairpin that rotates around itself, and the instability then proceeds in both directions (Fig. 5). This may result in the formation of either a tightly packed sphere or a double helix. At the site where the instability nucleates, the tube goes from nearly straight to maximally curved. The instability then propagates from this site to the rest of the tube (Figs. 2 and 5). The observed evolution may be due to a gradual change in the concentration of polymer molecules on the membrane.

All the coiled structures we observe are maximally curved already *as they form* and do not tighten up gradually, unlike the experiments reported by Sakurai *et al.* [11,12]. In quantitative terms, this means that the curvature of the tube central line, C, is $C \approx 1/r_0$, where r_0 is the radius of the tube. We have not noticed any preferred direction in the coiling process, i.e., the helicity did not have a preferential sign. However, helicity is not easily measurable with phase contrast microscopy, and therefore we cannot reach a definite conclusion regarding this issue.

In previously reported cases [11,15], coiling of myelin figures was attributed to surface adhesion. This is clearly not the case in our system, as demonstrated by the experiment illustrated in Fig. 3. The tip of a myelin figure, in the process of coiling, adhered to an air bubble, which we then moved. Movement of the bubble stretched the coil [Figs. 3(a–c)], until the latter reached a configuration in which all self-contact was lost [Fig. 3(c)]. Note also that the coil is stretched more or less homogeneously. Upon detachment from the bubble, the coil retracted as if it was an ordinary spring [Fig. 3(d–g)].

Had surface adhesion been the dominant mechanism, one would not expect the response of a coil to mechanical stretching to be homogeneous, but rather for it to come apart at the site of weakest contact. Furthermore, adhesion cannot create a restoring force. Thus, if the coil is stretched open so that no contact sites are left, the tube should ''forget'' that it was coiled. If the force exerted on the end of the tube is then released, adhesion would induce coil formation starting at one point and propagating to the rest of the tube (similarly to the original formation process). This is in stark contrast with

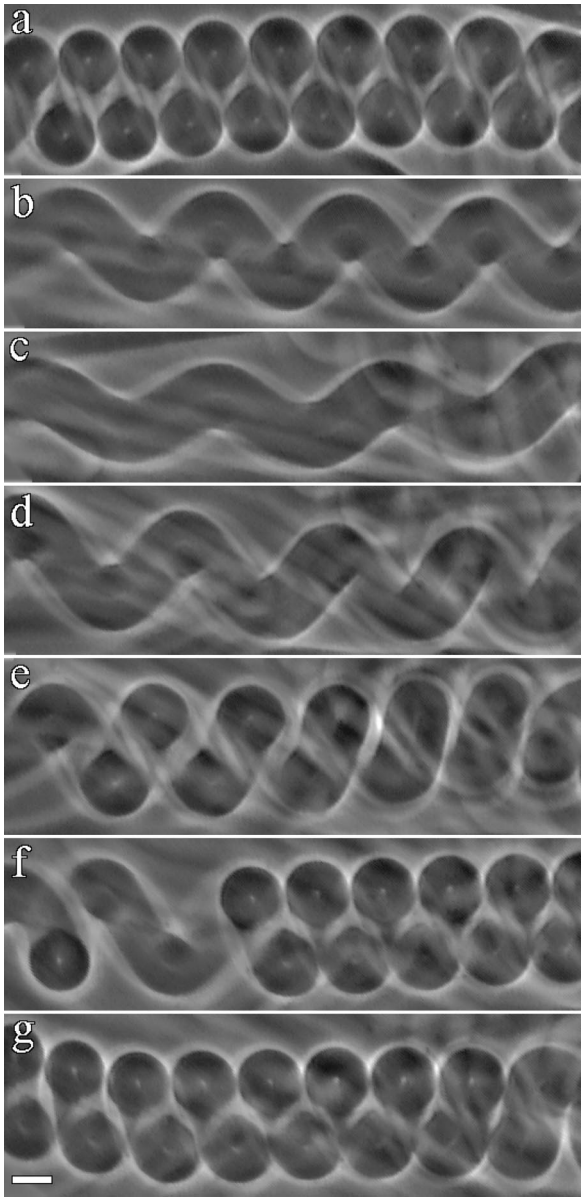

FIG. 3. A sequence of images depicting a single helix being mechanically stretched, and returning to a maximally curved configuration. The helix behaves like a spring, responding to the stretching force by elongating uniformly. When the force is removed the coil retracts. This behavior suggests a restoring force, rather than surface adhesion. Times are (a) before stretching, and (b) 67, (c) 102, (d) 159, (e) 215, (f) 325, and (g) 393 sec after initiation of stretching. Snapshots (d)–(g) were taken after the force was removed. The scale bar represents 10 μm.

our experimental observations.

Another piece of evidence against adhesion in our system is provided by the presence of many other structures in our experiments that come into contact with one another, but do not adhere. For example, Fig. 6(a) shows a double helix coming into contact with a myelin figure. The myelin figure is pushed aside when the double helix grows. This assures us that the two structures are indeed in contact. Despite the contact, the structures do not adhere, and after a few minutes they lose contact as can be seen in Fig. 6(b).

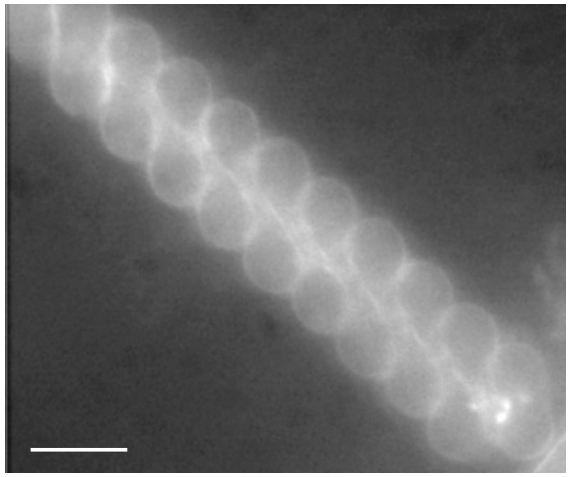

FIG. 4. Fluorescence image of a double helix. The scale bar represents 10 μm.

In order to understand better the role that the polymer plays in the coiling phenomenon, it is important to know its location in the membrane stack. For this purpose, fluorescence imaging was used. The results are shown in Fig. 7. As can be seen, the fluorescence intensity through the slice is concave. This is what one expects for a homogeneous polymer distribution throughout the stack, since in that case the intensity should be roughly proportional to the thickness of the tube in the microscope slice. From this we infer that the polymer is present, in significant quantity, throughout the myelin figure. Images of hollow tubes, where the polymer is predominantly on the outer layers, have a convex fluorescence intensity profile through their cross sections.

IV. THEORETICAL MODEL

We now present a simple theoretical model that captures most of the key experimental observations. For simplicity, we regard the system as if it were in equilibrium, effectively ignoring the slow evolution of the observed structures.

Consider a stack of concentric cylindrical sheets. We represent each bilayer as two square lattices (in the spirit of lattice-gas models), corresponding to the outer and inner monolayers. Each site represents a patch of membrane hav-

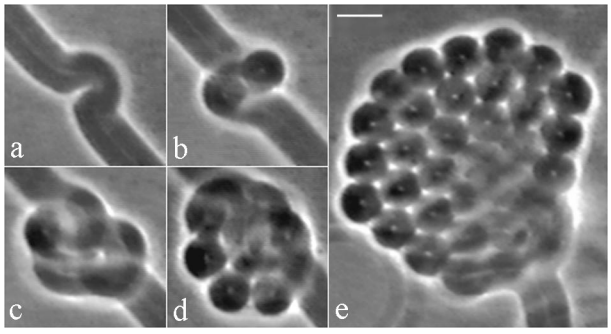

FIG. 5. Formation of a complex coil. The tube becomes unstable locally, forming a hairpin which gradually curls up. The intervals between snapshots (a)–(d) are 45 sec long. Structure (e) was observed 13 min after onset. The scale bar represents 10 μm.

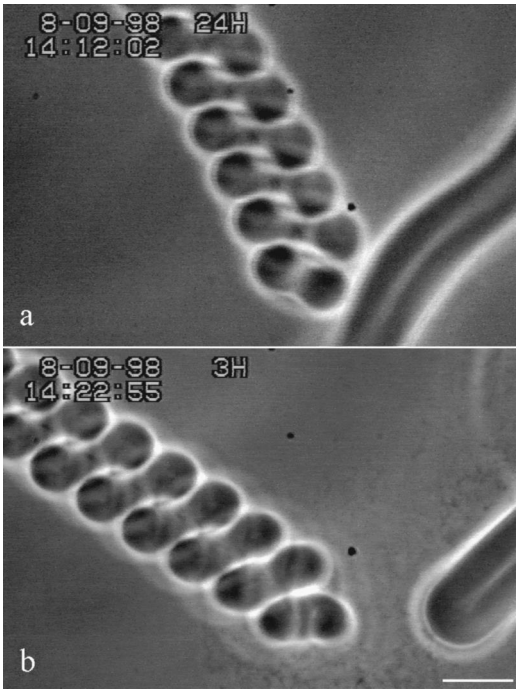

FIG. 6. A double helix coming into contact with another myelin figure. As the coil grows, it pushes the other figure aside. Fifteen minutes after initial contact, the two myelin figures are no longer touching. This is another demonstration that adhesion is not important in this system. The scale bar represents 10 μm.

ing area a^2, approximately the size of a polymer molecule performing a two-dimensional random walk on the membrane. Each lattice site has two degrees of freedom associated with it: the local mean curvature H and a binary occupation variable σ that takes the values 1 or zero when the site is occupied or unoccupied by a polymer molecule, respectively. To estimate the area of a site we assume that the hydrophilic backbone is in a good solvent (water) under semidilute conditions. This gives a radius of gyration $a \approx 40 - 80$ nm.

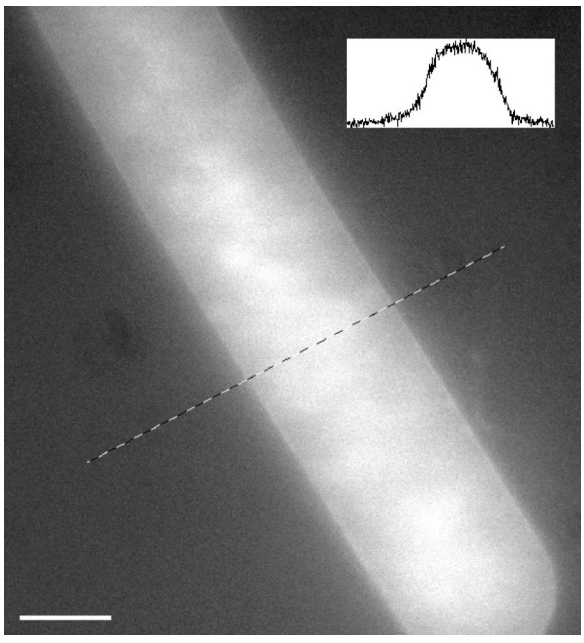

FIG. 7. Fluorescence image of a myelin figure showing that there is polymer inside. Inset: fluorescence intensity along the section. The scale bar represents 10 μm.

The energy of the system is a sum of the curvature energies of the sites $2\kappa H^2$ for a vacant site, and $2\kappa'(H-H_0)^2$ for a site occupied by a polymer. κ and κ' are the local bending rigidities of a monolayer without and with an attached polymer, respectively, and H_0 is the spontaneous curvature induced by the polymer. We assume that $H_0 > 0$, since the addition of polymer tends to bend membranes into shapes with higher curvatures. For the purpose of this simple model, the exact molecular mechanism responsible for this is not important. Possible mechanisms include the entropic pressure of the polymer backbone, or the incommensurability between the anchors and lipids. By convention, the curvatures of the inner and outer monolayers of the bilayer have opposite signs at the same position.

A crucial assumption is that polymer molecules can diffuse along the membrane, since the membrane is in a fluid state. In addition, we assume that the fluctuations of each membrane in a stack are severely restricted by the presence of its neighbors. As a result, there is a strong correlation between the transversal fluctuations throughout the tube. The myelin figure can thus be regarded as a flexible rod, having a circular cross section everywhere along its axis. The experimental pictures indeed display unchanging circular cross sections within experimental error.

Based on these assumptions, we developed a model that predicts that a high enough polymer concentration on the membrane can shift the equilibrium state from a straight tube to a maximally curved one. We first present a heuristic argument to show that if the spontaneous curvature H_0 is large enough, the free energy of a bent tube may be lower than that of a straight one. This approach may give a more intuitive understanding than the detailed calculations that follow.

A. Heuristic arguments

In order to find the equilibrium state of a tube, we have to calculate its free energy. This free energy depends on the curvature of its central line, C, and on the polymer concentration.

Consider one cylindrical bilayer of length l and circular cross section of radius r, with the same average polymer concentration ρ_0 on both sides. ρ_0 is defined as the number of polymer molecules on a monolayer, n, divided by the total number of sites on a monolayer, i.e., $\rho_0 = na^2/A$, where A is the total area of the membrane segment. Let us calculate the free energy cost of bending the bilayer into a portion of a coil with central line curvature C in three steps. First, we bend the tube while keeping the distribution of polymer around the tube homogeneous. Next, we allow the polymer to diffuse from regions of lower curvature to regions of higher curvature (Fig. 8), and finally we consider the entropy of mixing.

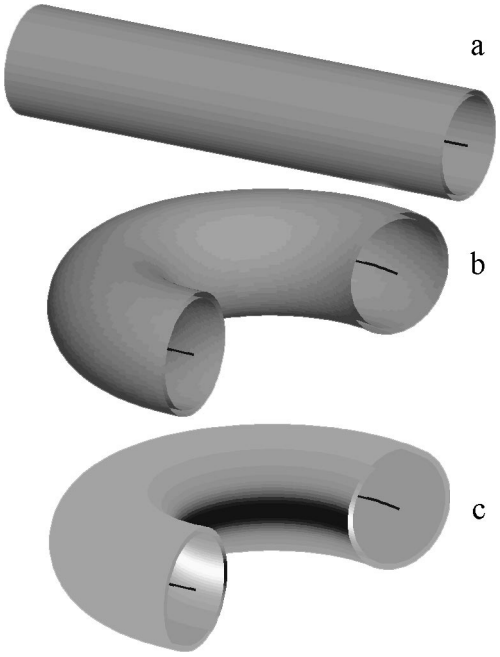

FIG. 8. Schematic representation of the heuristic argument. Starting from a straight tube with the same polymer concentration on the inner and outer monolayers (a), the cost of bending the tube keeping $\rho(\phi)$ homogeneous (b) is $E^{\pm}_{hom}$. Allowing the polymer to diffuse around the tube (c) to the configuration shown in Fig. 11 below lowers the energy by $\Delta E^{\pm}_{inhom}$, but also lowers the entropy. The black (white) color in (c) corresponds to areas of small (large) polymer concentration. Both E_{hom} and the entropy are independent of H_0, while $E^{\pm}_{inhom}$ is linear in H_0. Thus for large values of H_0 it is preferable to bend the tube.

The energy of a bent cylindrical bilayer with a *homogeneous* polymer distribution is $E_{hom}=E^{+}_{hom}+E^{-}_{hom}$, where E^{+}_{hom} and E^{-}_{hom} are the energies of the outer and inner monolayers, respectively. According to our model

$$E^{\pm}_{hom}(C)=2\rho_0\kappa'\int dA[H^{\pm}(C,\phi)-H_0]^2 + 2(1-\rho_0)\kappa\int dA[H^{\pm}(C,\phi)]^2, \qquad (1)$$

where ϕ is the angle around the tube, $H^{\pm}=\pm\frac{1}{2}[1/r + C\cos\phi/(1+Cr\cos\phi)]$ is the local membrane curvature, and $dA=d\phi(1+Cr\cos\phi)$. For simplicity, we shall assume here that $\kappa'=\kappa$. In the full model we allow the possibility that the presence of the polymer affects the local bending rigidity (i.e., $\kappa'\neq\kappa$).

For our geometry the total mean curvature obeys $\int dAH^{\pm}(C,\phi)=\pm 2\pi l$, independent of C. Thus the cost of bending the cylindrical membrane, keeping the polymer distribution homogeneous, is

$$\Delta E^{\pm}_{hom}\equiv E^{\pm}_{hom}(C)-E^{\pm}_{hom}(0) = 2\kappa\int dA[H^{\pm}(C,\phi)^2-H^{\pm}(0,\phi)^2]. \qquad (2)$$

From this it is obvious that there is always an energy cost to bend the tube in this way. However, the price is independent of the value of H_0.

Next, we take into account inhomogeneities in the distribution of polymer around the tube. Such inhomogeneities reduce the energy, if polymers move to regions of membrane curvature closer to H_0 in both the outer and inner monolayers. Rewriting Eq. (1) with ρ being now a function of ϕ we get

$$E^{\pm}_{inhom}(C)=2\kappa\int dA\rho^{\pm}_{\phi}[H^{\pm}(C,\phi)-H_0]^2 + 2\kappa\int dA[1-\rho^{\pm}_{\phi}][H^{\pm}(C,\phi)]^2, \qquad (3)$$

where $\rho^{\pm}_{\phi}$ are the polymer distributions on the outer and inner monolayers.

Subtracting Eq. (3) from Eq. (1), and taking into account conservation of polymer $\int dA\rho^{\pm}_{\phi}=\int dA\rho_0$, we see that the energy gain $\Delta E^{\pm}_{inhom}(C,H_0)\equiv E^{\pm}_{hom}(C,H_0)-E^{\pm}_{inhom}(C,H_0)$ depends linearly on the spontaneous curvature:

$$\Delta E^{\pm}_{inhom}=4\kappa H_0\int dA[\rho_0-\rho^{\pm}_{\phi}]H^{\pm}(C,\phi). \qquad (4)$$

Thus, for any polymer distribution with $\int\rho^{\pm}_{\phi}H(C,\phi)dA < \int\rho_0 H(C,\phi)dA$, the inhomogeneity lowers the energy; i.e., $\Delta E^{\pm}_{inhom}$ is positive and can become arbitrarily large for large values of H_0. The detailed calculation (see below) shows that such configurations indeed exist.

As for the entropy of the system, we assume that the dominant contribution is the entropy of mixing of the polymers and lipids. This entropy is larger when the distribution of polymers around the cylindrical bilayer is homogeneous, favoring a straight tube. However, it does not depend on the spontaneous curvature. Therefore, if H_0 is large enough, the energy gain due to $\Delta E^{\pm}_{inhom}(C,H_0)$ is larger than the free energy cost coming from $\Delta E^{\pm}_{hom}$ and the entropy of mixing. In this case, the tube is bent at equilibrium. It remains to be shown that such an equilibrium state can occur for reasonable and physical values of the model parameters. For this purpose we now turn to the full calculation.

B. Mean-field calculation

We neglect fluctuations of the central line curvature C, and correlations between different segments of the tube. A section of tubular bilayer of radius r and length l, with circular cross section having a fixed central line curvature C has an energy $E=E^{+}+E^{-}$, where E^{+} and E^{-} denote the energy of the outer and inner leaflets, respectively. $E^{\pm}$ take the form

$$E^{\pm}=2a^2\sum_{i,j}[\kappa(1-\sigma^{\pm}_{ij})+\kappa'\sigma^{\pm}_{ij}]\left(\frac{1}{r}G^{\pm}(\phi_i)-\sigma^{\pm}_{ij}H_0\right)^2, \qquad (5)$$

where $i=0,\ldots,2\pi r/a-1$ is the index around the tube and $j=0,\ldots,(l/a)(1+Cr\cos\phi_i)$ is the index along the tube (Fig. 9). $\sigma^{\pm}_{ij}=0,1$ are the occupation variables of the polymer

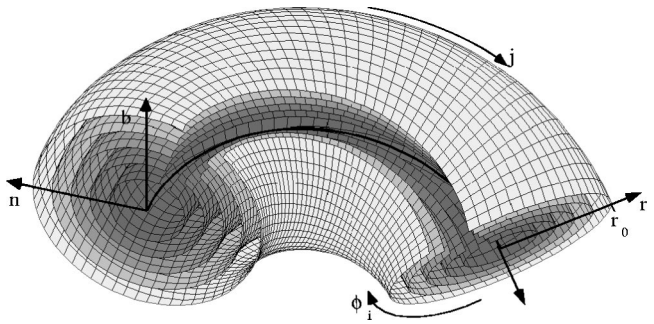

FIG. 9. A small section of a coiled stack of concentric membranes showing the directions of the normal $\vec{n}$ and the binormal $\vec{b}$. Each monolayer, having a radius r, is divided into patches with running indices i and j.

on the outer and inner monolayers, respectively, and $G^{\pm}(\phi_i)=\pm\frac{1}{2}[1+Cr\cos\phi_i/(1+Cr\cos\phi_i)]$, i.e., $G^{\pm}(\phi_i)/r$ is the local mean curvature of site (ij). $\phi_i=(a/r)i$ is the angle around the tube as shown in Fig. 9. By this convention the curvature of a site on the outer leaflet has the same magnitude as and opposite sign to the corresponding site on the inner leaflet.

To find the partition function, as a function of the average polymer occupation, we sum over the polymer degrees of freedom:

$$\Xi^{\pm}=\sum_{\{\sigma_{ij}^{\pm}=0,1\}}\exp\left(-\beta E^{\pm}+\beta\sum_{i,j}\mu^{\pm}\sigma_{ij}^{\pm}\right). \tag{6}$$

The second term in the exponent is a Lagrange multiplier that allows us to set the average concentrations on the membrane, $\rho_{\pm}=\Sigma_{i,j}\sigma_{ij}^{\pm}/N$, to the desired value by adjusting the chemical potentials $\mu^{\pm}$. N is the total number of sites per monolayer. Note that $\rho_{\pm}$ is the average of $\rho_{\phi}^{\pm}$. From this we calculate the free energy:

$$F^{\pm}(C,\rho)=-K_BT\ln(\Xi^{\pm})+\mu^{\pm}N\rho_{\pm}. \tag{7}$$

The summation over the polymer occupation degrees of freedom can be carried out, leading to

$$\ln(\Xi^{\pm})=\frac{lr}{a^2}\int_0^{2\pi}d\phi(1+Cr\cos\phi)\ln[e^{-2\beta(a^2/r^2)\kappa[G^{\pm}(\phi)]^2}+e^{-2\beta a^2\kappa'[(1/r)G^{\pm}(\phi)-H_0]^2+\beta\mu^{\pm}}], \tag{8}$$

where the approximation $\Sigma_i\approx(r/a)\int_0^{2\pi}d\phi$ was used. This approximation is valid when the size of a patch is significantly smaller than the radius of the tube. We estimate that $a/r_0\approx10^{-2}$ in our system, allowing us to expand Eq. (8) in powers of a/r to second order, and evaluate the integral in Eq. (8):

$$\ln(\Xi^{\pm})=\frac{\pi l}{2r}\left[\frac{4r^2}{a^2}\ln(1+y^{\pm})-\frac{2\beta(\kappa+\kappa' y^{\pm}-4\beta a^2\kappa'^2H_0^2y^{\pm})}{(1+y^{\pm})\sqrt{1-(Cr)^2}}\pm\frac{8\beta\kappa' rH_0y^{\pm}}{1+y^{\pm}}-\frac{8\beta^2\kappa'^2a^2H_0^2y^{\pm 2}}{(1+y^{\pm})^2\sqrt{1-(Cr)^2}}\right], \tag{9}$$

where $y^{\pm}=\exp(\beta\mu^{\pm}-2\beta\kappa' a^2H_0^2)$.

We are interested in finding the free energy as a function of the polymer concentration on the membrane, $\rho_{\pm}$, rather than the chemical potential $\mu^{\pm}$. Using

$$\frac{\partial\ln(\Xi^{\pm})}{\partial(\beta\mu^{\pm})}=\frac{2\pi lr}{a^2}\rho_{\pm}, \tag{10}$$

we get

$$\rho_{\pm}=\frac{y^{\pm}}{1+y^{\pm}}\pm\frac{2\beta\kappa' a^2H_0y^{\pm}}{r(1+y^{\pm})^2}+O\left(\frac{a^2}{r^2}\right). \tag{11}$$

Solving for $y^{\pm}$ gives $y^{\pm}=\rho_{\pm}[1\mp2(a/r)\beta\kappa' aH_0]/(1-\rho_{\pm})$ to second order in a/r. Substituting this into Eq. (7) and subtracting the energy for forming the straight tube, $F^{\pm}(0,\rho_{\pm},r)$, we get the free energy cost of bending a single bilayer of radius r within the stack:

$$F^{\pm}(C,\rho_{\pm},r)-F^{\pm}(0,\rho_{\pm},r)=\frac{\pi l}{r}[\kappa+(\kappa'-\kappa-4\beta\kappa'^2a^2H_0^2)\rho_{\pm}+4\beta\kappa'^2a^2H_0^2\rho_{\pm}^2]\times\left[\frac{1}{\sqrt{1-(cr)^2}}-1\right]. \tag{12}$$

The free energy cost of bending the entire tube is then the integral of Eq. (12) over the stack. In general, $\rho_{\pm}$ are functions of r. As we do not know the form of this function, we assume for simplicity that the average polymer concentration is the same on all the monolayers of the stack, i.e., $\rho_{\pm}(r)=\rho_0$. Variations in $\rho_{\pm}$ with r do not qualitatively change our conclusions. Under this assumption the free energy cost of bending the tube is

$$f(C,\rho_0)=\frac{1}{d}\int_0^{r_0}dr[F^{+}(C,\rho_0,r)-F^{+}(0,\rho_0,r)+F^{-}(C,\rho_0,r)-F^{-}(0,\rho_0,r)]=\frac{2l\kappa_{tube}(\rho_0)}{r_0^2}\ln\left[\frac{2}{1+\sqrt{1-(Cr_0)^2}}\right], \tag{13}$$

where $\kappa_{tube}=(\pi r_0^2/d)[4\beta\kappa'^2a^2H_0^2\rho_0^2+(\kappa'-\kappa-4\beta\kappa'^2a^2H_0^2)\rho_0+\kappa]$, and d is the bilayer spacing in the stack.

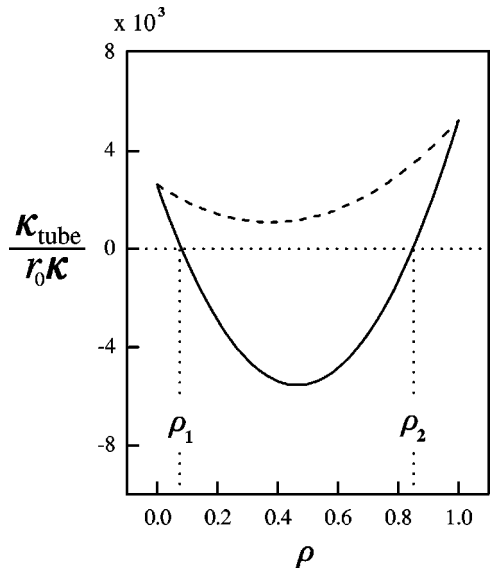

FIG. 10. The effective bending modulus of the tube, κ_{tube}, is parabolic in the average occupancy ρ. We have used the following values of the parameters: $\kappa=10k_BT$, $\kappa'=2\kappa$, and $r_0=5$ μm. We find that κ_{tube} depends on a and H_0 only through the product aH_0. The solid curve represents κ_{tube} for $aH_0=0.3$. When aH_0 is large enough ($aH_0>0.19$ for the values of κ and κ' we have used), $\kappa_{tube}<0$ between ρ_1 and ρ_2. For smaller values of aH_0, $\kappa_{tube}>0$ for all values of ρ. The dashed curve corresponds to $aH_0=0.16$.

The logarithm in Eq. (13) is an increasing function of C. Thus the behavior of the tube is dictated by the sign of the effective bending modulus of the tube, κ_{tube}. If it is positive, the minimum of $f(C,\rho_0)$ is at $C=0$, and tubes are straight on average. If, on the other hand, $\kappa_{tube}<0$, tubes form tight coils, since the minimum of the free energy is at the maximal possible central line curvature $C=1/r_0$. In this case, the free energy of the tube decreases upon bending, in agreement with our qualitative argument (see above).

The typical dependence of κ_{tube} on ρ_0 for large enough values of H_0 is shown in Fig. 10 as a solid line. When $\rho_0<\rho_1$, κ_{tube} is positive and decreases with ρ_0. In this regime the tube is predicted to be straight on the average, but with enhanced fluctuations due to the smaller bending modulus. Although we assumed that the presence of polymer molecules increases the local bending rigidity of the membrane ($\kappa'>\kappa$), their mobility makes it *easier* to bend the tube.

For $\rho_1<\rho_0<\rho_2$, κ_{tube} is negative and the tubes form *maximally tight* coiled structures. ρ_1 is therefore a threshold occupancy above which straight tubes are unstable. Above ρ_2 straight tubes become stable again. However, this regime is probably unreachable in our experiments, since too large a polymer concentration destroys the bilayers.

For small values of H_0, κ_{tube} is always positive and the model does not predict a coiling instability (dashed line in Fig. 10). Therefore, we now check whether the experimental values of the various parameters correspond to a regime in which a coiling instability is predicted. Using pipet aspiration [19] we measured the bending modulus of a bilayer to be $2\kappa\simeq 20\pm 5k_BT$. We assume that $H_0>10$ μm^{-1} because we have observed objects that have radii of curvature of the order of or smaller than optical resolution (~ 0.2 μm). We suppose $\kappa'>\kappa$; this is consistent with models of composite membranes [20–22] (although the systems these models describe are different from ours), and with experiments (Evans and Rawicz measured $\kappa'\simeq 2\kappa$ for membranes with grafted polymers [19]). Putting these estimates into Eq. (13) we see that even for small amounts of polymer κ_{tube} can become negative ($\rho_1\leqslant 0.1$), leading to a coiling instability.

The model predicts an inhomogeneous polymer concentration around the tube, which we now wish to calculate. In the expression for Ξ one can use a ϕ-dependent chemical potential $\mu_\phi^\pm$. The distribution of polymer around the bent tube is then calculated as follows:

$$\rho_\phi^\pm=\frac{d\ln(\Xi^\pm\{\mu_\phi^\pm\})}{d(\beta\mu_\phi^\pm)}=\frac{1}{1+\exp[-2\beta(a^2/r^2)\kappa G^\pm(\phi)^2+2\beta a^2\kappa'[G^\pm(\phi)/r-H_0]^2-\beta\mu^\pm]}. \tag{14}$$

The chemical potentials $\mu^\pm$ corresponding to a particular total concentration $\rho_\pm$ were found numerically by plotting the integral of Eq. (14) over ϕ, as a function of $\mu^\pm$. The value of $\mu^\pm$ corresponding to the desired $\rho_\pm$ was then read from the graph. Using it in Eq. (14), we calculated $\rho_\phi^\pm$. Examples of such distributions are shown in Fig. 11.

V. IMAGING MODEL

The model of the previous section predicts maximally curved coils, i.e., $C=1/r_0$, for $\rho_1<\rho_0<\rho_2$. In order to test this prediction we analyzed the experimental pictures in detail. The images obtained from the microscope are two-dimensional projections of the viewed object, and include contributions from regions that are out of focus. Phase contrast microscopy complicates the interpretation of the images further, since the intensity at a particular point is not a monotonic function of the amount of material that the rays of light traverse. This can create apparent defects, as illustrated in Fig. 12, and makes resolving images such as Fig. 5(e) very difficult.

In order to test the theoretical predictions, we have used numerical simulations of various coils to derive virtual projections, and compared them with the experimental images. The simplest objects we considered are ideal single and double helices. We calculated a geometrical phase diagram

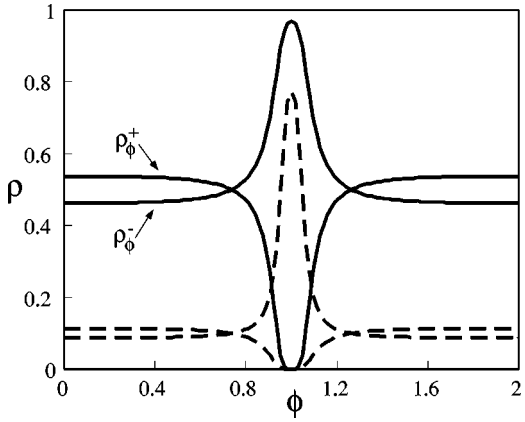

FIG. 11. The local polymer concentration as a function of the angle around the tube is shown for two average polymer concentrations, $\rho=0.5$ (solid lines) and $\rho=0.1$ (dashed lines). The following parameters have been used: $r/a=100$, $rC=0.99$, $aH_0=0.3$, $\kappa=10k_BT$, $\kappa'=2\kappa$.

for the different possible types of single and double helices and their curvatures and lines of contact, as described in the Appendix. Finally, we considered complex coils reminiscent of the complex structures seen in many of our experiments.

By generating simulated curves we can see the effects of various imaging parameters on the resulting image. For example, when the coil under observation crosses the focal plane, its shape seems to change from a symmetrical arrangement to a series of parallel streaks. This is shown in Fig. 13, where an experimental image is compared with a simulated ideal helix rotated by 10° with respect to the imaging plane. In another case, the image gives the impression of a helicity reversal as illustrated in Fig. 12, even though the helix is ideal. A similar effect is seen when a myelin figure is slightly curved. This demonstrates that even slices of very simple objects may display complex features. Therefore, it is extremely difficult to reconstruct the objects that correspond to the experimental images.

Could the tight complex coils observed experimentally (Fig. 5) have maximal central line curvature everywhere? In view of the difficulties outlined above, we can only partially answer this question. In order to fully define a curve in three-dimensional space, two parameters have to be specified at every point. One choice for such parameters is the curvature C and the torsion τ. Our theory predicts that $C=1/r_0$ when $\rho_1<\rho<\rho_2$. It does not, however, specify what τ should be. We investigated various shapes with $C\approx 1/r_0$ and varying τ using a numerical simulation. The program takes two known functions for C and τ, and integrates them to form a three-dimensional curve. Concentric cylinders are then drawn around this curve. The resulting object can then be rotated and sliced. Such a slice represents to a certain extent the depth of focus of the microscope. The resulting image is then smoothed using a Gaussian filter, in order to remove the underlying grid, and compared to an experimental image.

An example of this procedure is illustrated in Fig. 14. The best fit that we found to the experimental object shown at the top is displayed at the bottom. This is a maximally curved double helix with a complex (though periodic) torsion. It

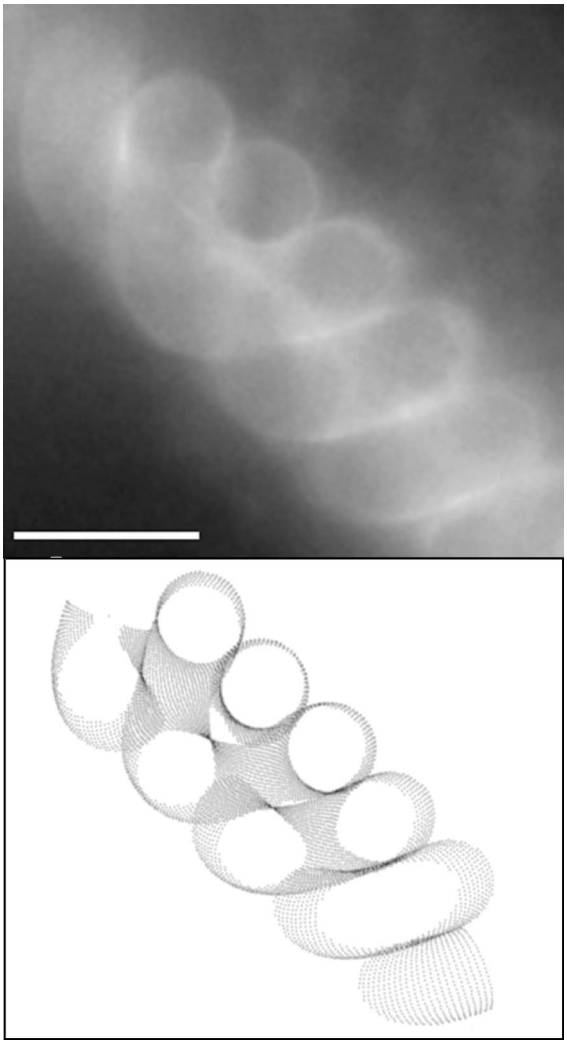

FIG. 12. Top: Fluorescence image of a double helix showing that the helicity seems to reverse where the coil intersects the focal plane. This is an artifact of the imaging geometry, as can be seen for the theoretical *ideal* double helix tilted at 15° at the bottom. The scale bar represents 10 μm.

may be possible to generate more complex maximally curved coils, similar to those observed [see Fig. 5(e)], using a nonperiodic torsion. However, it is difficult to simulate such objects because of the difficulty in enforcing excluded volume constraints. Thus, we can only simulate the simplest structures observed experimentally. The curvatures of these structures are consistent with the prediction of the model; i.e., they are maximally curved.

VI. DISCUSSION

Our theory assumes that the observed structures are in equilibrium, and ignores their evolution. This is justified for many of the coiled structures, which evolve very slowly. In most cases, this slow evolution leads to growth of the coil as additional parts of the tube become curved. A nonequilibrium model is needed to account for this effect.

While our model explains the observed phenomena, other models have been proposed in the literature to explain coil-

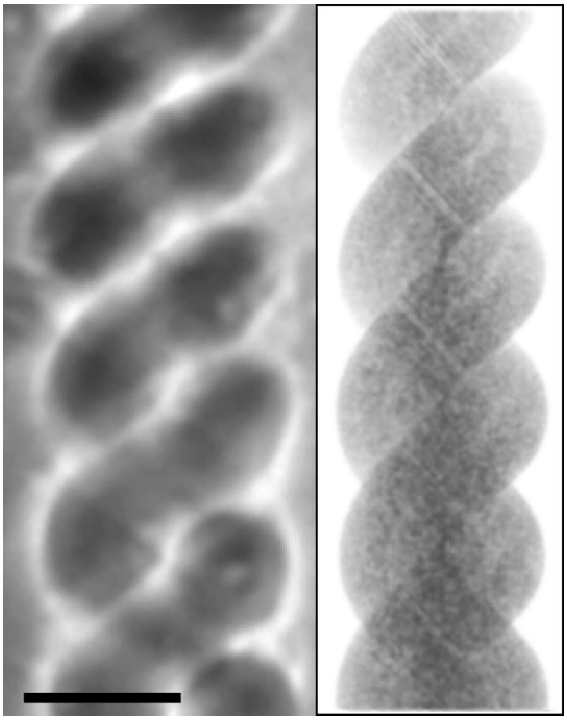

FIG. 13. A comparison between an experimental double helix (left) and a model ideal double helix (right). This image shows the effect of tilting the coil by 10° with respect to the imaging plane. Notice the cut has a symmetric appearance at the bottom, where the imaging plane slices through the center of the coil, shifting gradually toward an array of parallel smudges at the top. The scale bar represents 10 μm.

ing in other systems. The rest of the discussion is devoted to these other possibilities.

The coiling of DMPC-cardiolipin myelin figures was attributed to Ca^{2+}-mediated membrane-membrane binding [15]. Surface adhesion was also suggested as the dominant mechanism responsible for the coiling of egg-yolk lecithin myelin figures [13]. It was proposed that the gain in energy coming from surface adhesion overcomes the elastic energy required to bend the tube. Furthermore, it was postulated that by twisting back along its length a rod increases the length of the line of contact, thereby increasing the area of contact. An analysis of simple helices shows that this is not generally true. This is shown in the Appendix. First, there may be up to four lines of contact, depending on the type of double helix. Moreover, the length of the line of contact is not simply related to how tight the structure is. In fact the maximum length of the line of contact occurs when the two helices revolve around a large radius, thereby being effectively straight. In our system we have found strong evidence that surface adhesion does not play a dominant role in determining the morphology.

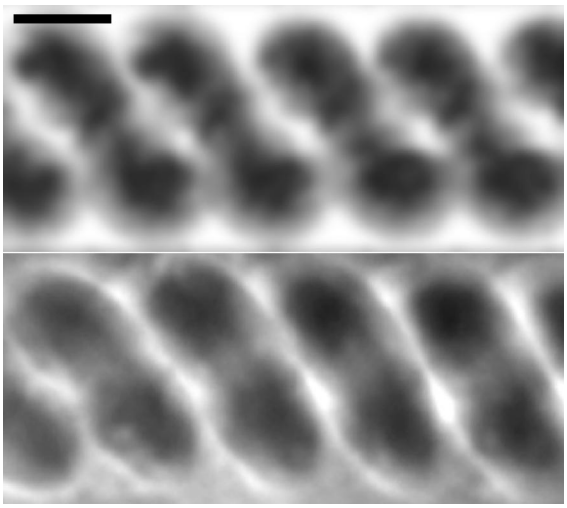

FIG. 14. Top: experimental image of a double helix. Bottom: cross section of a theoretical double helix having maximal curvature ($C=1/r_0$), and sinusoidal torsion $\tau=2+2\sin\{(2\pi/31)[i+1.8\sin(2\pi i/31+3\pi/2)]\}$. The central line of the image is shifted by r_0 below the imaging plane. The scale bar represents 10 μm.

A generalization of our model may be relevant to other multicomponent systems. For example, calcium is known to induce a lateral phase separation in a lipid mixture containing cardiolipin, thereby creating an inhomogeneous distribution. Egg-yolk lecithin is also a mixture of lipids with the same head group and a variety of tail lengths and degrees of saturation [14].

Another type of curvature model—the area difference elasticity (ADE) model—has been discussed in the literature [23]. In this approach it is assumed that each monolayer has a certain preferred area. If there is an area difference between the monolayers comprising a bilayer, then the bilayer will bend in order to accommodate it. In effect ADE and spontaneous curvature both predict the same equilibrium shapes for hollow vesicles. However, ADE cannot explain the coiling of myelin figures. This is because bending a tube, so that it is part of a torus, does not change its area. This is true for each monolayer in the stack, and, in particular, the area difference between layers is unchanged.

We believe coiling occurs mainly due to the spontaneous curvature induced by the presence of the polymer molecules as well as their mobility. Our model emphasizes these aspects, and neglects others such as membrane distortions due to the polymer backbone and interactions between polymers. We do not expect these effects to change the qualitative behavior of the system.

ACKNOWLEDGMENTS

We thank especially L. Jullien, for his help and encouragement. We also acknowledge useful exchanges with R. Lipowsky, E. Moses, and S. Safran. This research was supported by The Israel Science Foundation administered by the Israel Academy of Sciences and Humanities—Recanati and IDB Group Foundation, and The Minerva Foundation.

APPENDIX: GEOMETRIC PHASE DIAGRAM

The requirement that a physical coil does not intersect itself imposes a constraint on the relation between the pitch and the radius of a helix. This constraint, as well as the lines of contact, are now calculated for single and double helices.

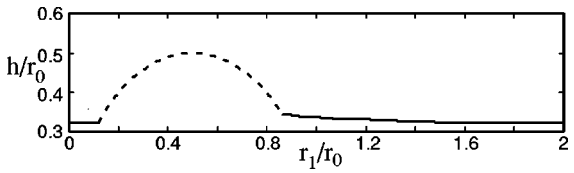

FIG. 15. The line of self-contact for single helices. r_0 is the outer radius of the tube. $2\pi h$ and r_1 are the pitch and the radius of the central line of the helix, respectively. The requirement that a physical coil does not intersect itself gives two conditions. The dashed line corresponds to the first condition, while the solid lines corresponds to the second condition, as explained in the text.

Some of the helices studied here were considered also in [24–27].

1. Single helix

The central line of a helical tube can be parametrized as follows:

$$\vec{R}_1(t)=(r_1\cos(t),r_1\sin(t),ht), \tag{A1}$$

where r_1 is the radius of the helix around the z axis, $2\pi h$ is the pitch, and t is a parameter running along the curve. From this we see that the curvature is $C=r_1/(r_1^2+h^2)$, while the torsion is given by $\tau=h/(r_1^2+h^2)$.

A myelin figure is then represented by drawing a stack of concentric tubes having a circular cross section around this line:

$$\vec{R}(t,\theta)=\vec{R}_1(t)+r[\vec{n}(t)\cos(\theta)+\vec{b}(t)\cos(\theta)], \tag{A2}$$

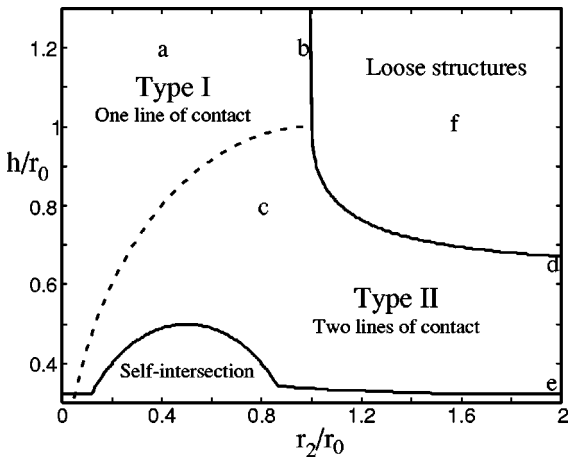

FIG. 16. Geometrical phase diagram for double helices. r_0 is the outer radius of the tubes and $2\pi h$ is the pitch of the central line of the two helices. r_1 and r_2 are the radii of the central lines of the two helices. Our convention is that $r_2 \leqslant r_1$. There are two types of geometry, separated by the dashed line in the figure, type I, two helices winding around each other, and type II, interlaced helices revolving around a central hole. The lower bound is the limit below which a helix intersects itself. The top right bound is the line of symmetry, where both helices have the same radius.

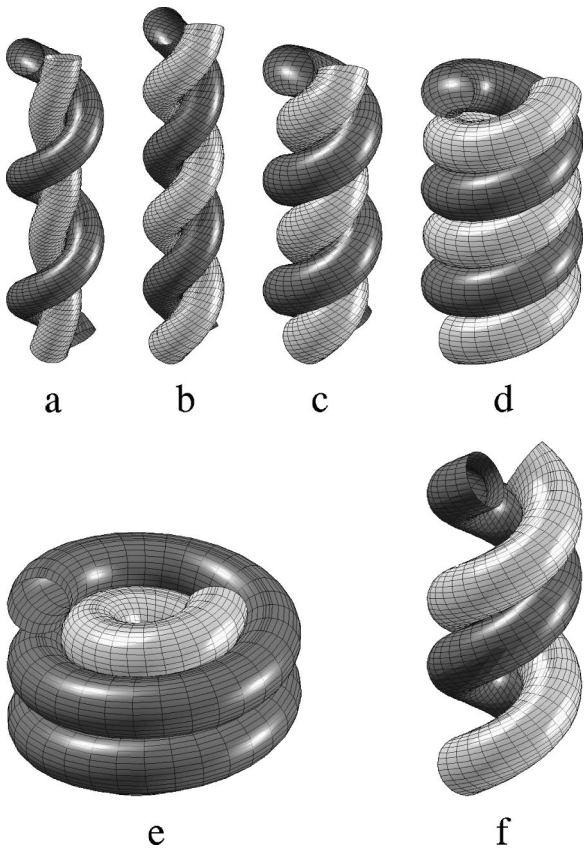

FIG. 17. Simulations of representative ideal theoretical helices. Letters are keyed to the diagram in Fig. 16. Most of the double helices observed experimentally resemble type (c), although some of them are more symmetric than the example shown.

where $\vec{n}(t)$ and $\vec{b}(t)$ are the normal and binormal to the curve at point t and $0<r\leqslant r_0$ as shown in Fig. 9. The demand that a physical tube does not intersect itself yields two conditions.

(1) The curvature of the central line $C\leqslant 1/r_0$. At $C=1/r_0$ two consecutive segments along the tube come into contact. From this condition we find that $h\geqslant\sqrt{r_1(r_0-r_1)}$.

(2) The pitch of the coil must be such that a segment of the coil does not intersect any previous segment. This requirement can be checked numerically by determining the distance between any two points along the curve, and demanding that this distance be greater than or equal to $2r_0$. The result is another constraint on $h(r_0,r_1)$. Helices for which this distance equals $2r_0$ have a contact line that is a helix with the same radius and pitch as the central line, but shifted by r_0 along the line of symmetry. The allowed parameters are summarized in Fig. 15 (see also [27]).

2. Double helices

We consider a double helix as two single helices, having radii r_1 and r_2, that have at least one continuous line of contact. If there is no such contact then they are simply two unconnected single helices. For simplicity we assume that both tubes have the same radius r_0 around their respective central lines, and that these central lines wind around the z

axis. The line of contact is itself a helix with the same pitch, and with a radius $r_2 \leqslant r_{con} \leqslant r_1$. The constraint of having a distance of $2r_0$ between the two central lines allows us to find r_1 as a function of r_2 and h.

There are two types of double helices. Type I double helices have $h > \sqrt{r_2(2r_0 - r_2)}$. In this case, the two helices wind around their line of contact and their radii obey $r_1 = 2r_0 - r_2$. Double helices of type II obey the condition $h < \sqrt{r_2(2r_0 - r_2)}$. In this case, the coils are intermingled and wind around a hole in the middle. This is summarized as a phase diagram in Fig. 16. Type II double helices have at least two lines of contact [an example is shown in structure (d) of Fig. 17].

We now find the lines of contact between the two coils of a double helix. Using Eq. (A1) we define the central lines of the two strands:

$$\vec{R}_1(t_1) = (r_1 \cos(t_1), r_1 \sin(t_1), ht_1),$$
$$\vec{R}_2(t_2) = (r_2 \cos(t_2 + \eta), r_2 \sin(t_2 + \eta), ht_2). \tag{A3}$$

The phase η is $\eta = \pi$ for double helices of types I and II, and for loose helices η is determined by the requirements that there exists at least one line of contact. The line of contact is then given by $\vec{D}(t_1, t_2) = \vec{R}_1(t_1) - \vec{R}_2(t_2)$. From the requirement that $\vec{D} \perp \partial \vec{R}_i / \partial t_i$ and that $|\vec{D}| = 2r_0$ we find that the line of contact is a helix with the same pitch as the other two helices, and a radius

$$r_c = \frac{1}{2}\sqrt{r_1^2 + r_2^2 - 2r_1 r_2 \cos(\Delta)}, \tag{A4}$$

where $\Delta = (b/d - 2 \pm 2\sqrt{1 - b/d + 1/d^2})^{1/2}$, $d = h^2/(r_1 r_2)$, and $b = (4r_0^2 - r_1^2 - r_2^2)/(r_1 r_2)$.

Double helices of type I have one line of contact, while type II helices typically have two lines of contact. At the dotted line in Fig. 16 the two lines merge. Type II helices lying on the line of self-intersection also have lines of self-contact, for a total of four lines of contact. The maximal length of contact lines occurs when one helix lies within the other and their radii go to infinity. In this case the total length of contact is four times the length of the central line of each helix. Thus, formation of a tighter helix does not necessarily mean that the line of contact increases, not to mention the area of contact. The area of contact between two cylinders depends on the angle at which they come into contact. Moreover, when there are two lines of contact close together (for example, near the dotted line in Fig. 16) the areas of contact must overlap to some degree.

[1] O.-Y. Zhong-can and Z.-B. Su, Phys. Rev. Lett. **78**, 4055 (1997).
[2] N. R. Cozzarelli, C. Boles, and J. H. White, in *DNA Topology and Its Biological Effects*, edited by N. R. Cozzarelli (Cold Spring Harbor Laboratory, Cold Spring Harbor, NY, 1990).
[3] A. Goriely and M. Tabor, Phys. Rev. Lett. **80**, 1564 (1998).
[4] I. Klapper, J. Comput. Phys. **125**, 325 (1996).
[5] V. Frette, M. Guedeau-Boudeville, I. Tsafrir, L. Jullien, D. Kandel, and J. Stavans, Phys. Rev. Lett. **83**, 2465 (1999).
[6] H. Ringsdorf, J. Venzmer, and F. M. Winnik, Angew. Chem. Int. Ed. Engl. **30**, 315 (1991).
[7] R. Virchow, Virchows Arch. **6**, 562 (1854).
[8] O. Lehmann, Sitzungber. Heidelberger Akad. Wiss. Math.-Naturwiss. Kl., Abt. A **13**, 1 (1913).
[9] M. Buchanan, J. Arrault, and M. E. Cates, Langmuir **14**, 7371 (1998).
[10] M. Buchanan, S. U. Egelhaaf, and M. E. Cates, Langmuir **16**, 3718 (2000).
[11] I. Sakurai, Y. Kawamura, T. Sakurai, A. Ikegami, and T. Seto, Mol. Cryst. Liq. Cryst. **130**, 203 (1985).
[12] I. Sakurai, T. Suzuki, and S. Sakurai, Biochim. Biophys. Acta **985**, 101 (1989).
[13] K. Mishima, K. Fukuda, and K. Suzuki, Biochim. Biophys. Acta **1108**, 115 (1992).
[14] N. H. Tattrie, J. R. Bennet, and R. Cyr, Can. J. Biochem. **46**, 819 (1968).
[15] K.-C. Lin, R. M. Weis, and H. M. McConnell, Nature (London) **296**, 164 (1982).
[16] I. Tsafrir, D. Sagi, T. Arzi, M. Guedeau-Boudeville, V. Frette, D. Kandel, and J. Stavans, e-print cond-mat/0004019.
[17] H. J. Deuling and W. Helfrich, Blood Cells **3**, 713 (1977).
[18] See http://www.weizmann.ac.il/~festava
[19] E. Evans and W. Rawicz, Phys. Rev. Lett. **79**, 2379 (1997).
[20] R. Lipowsky, Europhys. Lett. **30**, 197 (1995).
[21] C. Hiergeist and R. Lipowsky, J. Phys. II **6**, 1465 (1996).
[22] W. Helfrich and M. M. Kozlov, J. Phys. II **4**, 1427 (1994).
[23] L. Miao, U. Seifert, M. Wortis, and H. G. Dobereiner, Phys. Rev. E **49**, 5389 (1994).
[24] A. Stasiak, J. Dubochet, V. Katritch, and P. Pieranski, in *Ideal Knots*, edited by A. Stasiak, V. Katritch, and L. H. Kauffman (World Scientific, Singapore, 1998), Chap. 1.
[25] A. Maritan, C. Micheletti, A. Trovato, and J. R. Banavar, Nature (London) **406**, 287 (2000).
[26] A. Stasiak and J. H. Maddocks, Nature (London) **406**, 251 (2000).
[27] S. Przybyl and P. Pieranski (unpublished).